Photocatalytic Degradation of Deoxynivalenol Using Cerium Doped Titanium Dioxide under Ultraviolet Light Irradiation

Pengzhen He [1,2,†], Zhiyong Zhao [2,†], Yanglan Tan [3], Hengchao E [2], Minghui Zuo [1], Jianhua Wang [2], Junhua Yang [2], Shuxin Cui [1,*] and Xianli Yang [2,*]

1   College of Chemistry and Chemical Engineering, Mu Danjiang Normal University, Mu Danjiang 157012, China; hepengzhenadu@163.com (P.H.); minghuizuo@mdjnu.edu.cn (M.Z.)
2   Institute for Agro-food Standards and Testing Technology, Shanghai Academy of Agricultural Sciences, Shanghai 201403, China; zhaozhiyong@saas.sh.cn (Z.Z.); ehengchao@saas.sh.cn (H.E.); wangjianhua@saas.sh.cn (J.W.); yangjunhua@saas.sh.cn (J.Y.)
3   CAS Key Laboratory of Nutrition, Metabolism and Food Safety, Shanghai Institute of Nutrition and Health, Chinese Academy of Sciences, Shanghai 200031, China; yltan@sibs.ac.cn
*   Correspondence: shuxincui@mdjnu.edu.cn (S.C.); yangxianli@saas.sh.cn (X.Y.)
†   Both P.H. and Z.Z. rank as the first authors.

Abstract: Deoxynivalenol (DON) is a major mycotoxin with high toxicity that often contaminates grains, foods and feeds. The traditional approaches for DON removal are difficult to meet industry and agriculture demands due to the high stability of the DON molecule. Therefore, there is an urgent need to develop green and effective strategies for DON degradation. In this study, a batch of photocatalytic nanomaterials of cerium (Ce) doped titanium dioxide (TiO_2) were successfully prepared by sol-gel method. The catalysts were systematically characterized by XRD, HRTEM, FT-IR, UV-Vis and XPS. The catalyst 0.5Ce-TiO_2 showed superior photocatalytic activity for DON degradation in aqueous solution under ultraviolet light irradiation, better than that of traditional photocatalyst pure TiO_2, and 96% DON with initial concentration of 5.0 mg/L could be degraded in 4 h. In addition, the two possible degradation intermediate products $C_5H_8O_3$ and $C_{17}H_{18}O_6$ were identified, the photocatalytic degradation mechanism and degradation pathway were studied. The results indicate that Ce doped TiO_2 photocatalyst can be used to reduce DON effectively.

Keywords: deoxynivalenol; photocatalytic degradation; cerium doped titanium dioxide; mechanism; pathway

Key Contribution: 0.5Ce-TiO_2 showed superior photocatalytic activity for DON removal in aqueous solution under ultraviolet light irradiation.

1. Introduction

Deoxynivalenol (DON), a high-toxicity secondary metabolite produced by *Fusarium graminearum*, is one of the most common mycotoxins in grains [1], foods and feeds [2]. This mycotoxin poses a serious threat to human health and animals [3,4].

Some technologies have been employed to eliminate DON. Physical methods such as washing and grinding can reduce the content of DON in contaminated grains, but DON is transferred to some other by-products. Heat treatment for DON removal is very limited, due to the strong thermal stability of DON molecule [5]. Bretz et al. reported that the DON molecule could be decomposed under alkaline conditions and then neutralized by chemical agents [6]. Biological detoxification methods could efficiently reduce the toxicity of DON under mild conditions [7]. Yin et al. found a strain A16 isolated from wheat fields, and identified as *Devosia sp.*, which could survive and degrade DON in several conditions [8]. Although biological methods have good detoxification effects, the disadvantage is relatively long treatment time, which limits its further application. Therefore, developing a safe and

efficient strategy for DON degradation is the trend in food and other related industries and agricultures.

In recent years, more and more researchers have paid increasing attention in the field of photocatalytic technology with high efficiency, low energy consumption and mild reaction conditions for DON degradation [9]. Oxide semiconductor modified doping materials can effectively degrade DON under light conditions, such as ZnO, TiO_2, etc. Wang et al. prepared photocatalytic materials dendritic-like α-Fe_2O_3, which could reduce 90.3% DON with initial concentration of 4.0 $\mu g/mL$ in an aqueous solution [10]. Bai et al. found the photocatalyst graphene/ZnO hybrids GZ0.3 prepared by a simple one-step hydrothermal method showed good ability to degrade DON in an aqueous suspension under ultraviolet light (UV) light irradiation. Zhou et al. reported a nanoparticles photocatalyst Tm@TiO_2 composite (UCNP@TiO_2), which was employed to reduce DON under the simulated sunlight [11]. Additionally, Wu et al. utilized upconversion nanoparticles@TiO_2 composites UCNP@TiO_2 to degrade DON in wheat.

Compared to other oxide semiconductor photocatalysts, TiO_2 as a non-toxic and environmentally friendly nanomaterial with good catalytic degradation of harmful substances has received extensive attention [12]. However, the wide band gap energy of TiO_2 with about 3.2 eV reduces the efficiency of light utilization and weakens its photocatalytic degradation ability [13]. Metal doping is one of the effective control strategies to enhance the photocatalytic activity by reducing the band gap energy of TiO_2 [14], which also could inhibit rapid recombination of photogenerated electron-hole pairs and broaden light absorption range redshift due to doping ions in TiO_2, making it possible to form complexes with Lewis bases such as organic acids or alcohols [15]. Cerium (Ce), as a rare earth element, is relatively nontoxic and cheaper than other rare earth metals. It was doped with TiO_2 to form a new composite catalysts and can effectively reduce the band gap energy of materials and have better catalytic degradation performance [16].

In this study, we successfully synthesized photocatalytic nanomaterials Ce doped TiO_2 by sol-gel method. The obtained 0.5Ce-TiO_2 showed superior photocatalytic activity for DON removal under ultraviolet light irradiation (λ = 254 nm) in an aqueous solution compared with traditional photocatalyst pure TiO_2. In addition, the possible degradation intermediate products were identified, and the photocatalytic degradation mechanism and degradation pathway were studied.

2. Results and Discussion

2.1. Structural Characterizations

2.1.1. Morphology Analyses and Crystal Phase

HRTEM Images and XRD Analysis

In order to study the microstructure and crystal phase composition of Ce doped TiO_2 catalytic materials, High Resolution Transmission Electron Microscope (HRTEM) were used to characterize the prepared catalytic materials. X-ray diffraction (XRD) was conducted to determine the phases and crystal structures of pure TiO_2, xCe-TiO_2(x = 0.5, 1, 5, 10, 20, 40) and CeO_2. The results are shown in Figure 1.

Figure 1a shows the morphology of the pristine TiO_2 particles with tiny spherical shapes. Ce doped TiO_2 shapes appearance becomes uniform and regular with doping Ce, shown in Figure 1b–h. Figure 1j displays the clear lattice fringes of 0.5Ce-TiO_2 with the particle size of approximately 24 nm. The interplanar distance of approximately 0.35 nm corresponds to the (101) crystal plane of anatase TiO_2, and the lattice fringe spacing is about 0.19 nm, corresponding to the (220) crystal plane of anatase TiO_2. Then, the particle size of TiO_2 doped with 0.5% Ce is about 24 nm, as seen in Figure 1i. Figure 1i shows the morphology of the pristine CeO_2 particles.

Figure 1i shows that the distinct diffraction peaks at 25.4, 37.9, 48.5, 55.1, 62.8, 68.8, 75 and 82.5° correspond to the (101), (004), (200), (211), (204), (116), (215) and (224) crystal planes of anatase TiO_2, while the diffraction peaks at 47.4 respond to the (220) planes of the cubic CeO_2. For the different Ce doping, the XRD patterns demonstrate a similar pattern

dominated by anatase, and no other phases can be observed, which is consistent with the HRTEM images. The results are different from previous reports, which showed the formation of the cerium titanate $Ce_2Ti_2O_7$ phase with Ce:Ti = 50% in molar ratio [17]. Most of the Ce ions cannot enter the TiO_2 lattice because the radius of Ce^{4+} is larger than that of Ti^4, and Ce dopant have been well dispersed on the surface of TiO_2 as the form of cerium oxide [18], which may be the reason why CeO_2 phases cannot be observed. In addition, the Ce doping expands the TiO_2 lattice, causing a large lattice distortion and strain energy. In order to compensate the lattice stress, the oxygen atoms on the TiO_2 surface escape the lattice to form oxygen vacancy, playing a role of trapping holes. The effect may contribute to reduce the probability of recombination of holes and electrons in TiO_2 and to increase the photocatalytic activity. The main peak (101) broadens with the increase of Ce content, and even disappears, suggests Ce doping inhibits the crystal growth and decreases the crystallinity of the synthesized materials.
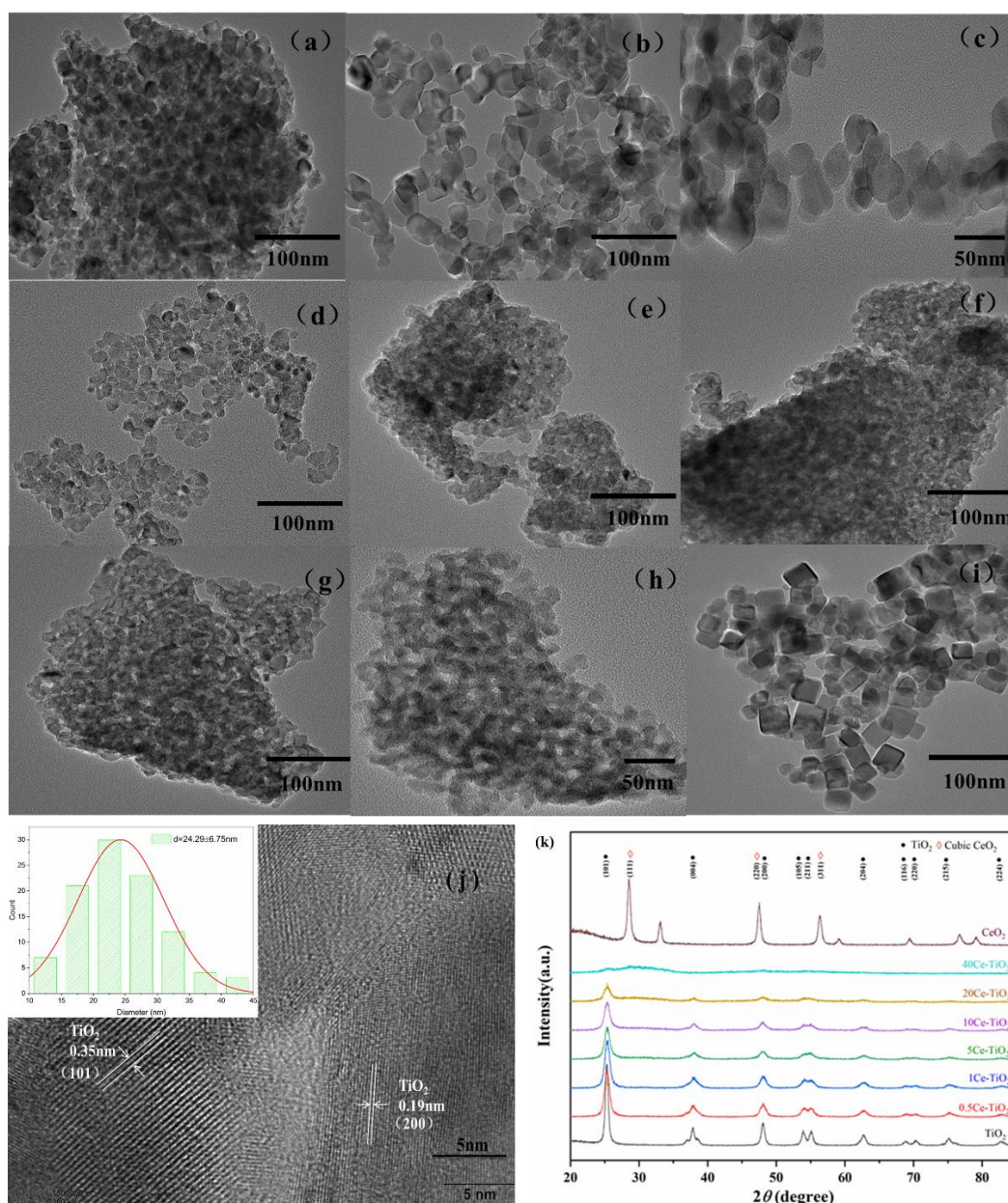
Figure 1. HRTEM images of catalyst prepared by sol-gel method: (**a**) TiO_2, (**b,c,j**) 0.5Ce-TiO_2, (**d**) 1Ce-TiO_2, (**e**) 5Ce-TiO_2, (**f**) 10Ce-TiO_2, (**g**) 20Ce-TiO_2, (**h**) 40Ce-TiO_2, (**i**) CeO_2 and (**k**) XRD patterns of as-prepared nanocomposites Ce doped TiO_2, TiO_2 and CeO_2.

XPS Analysis

The high resolution XPS spectra were performed to analyze and determine the chemical state of the synthesized Ce-doped TiO_2 photocatalyst. All the obtained spectra were calibrated to the C 1s electron peak at 284.6 eV. The results are shown in Figure 2.
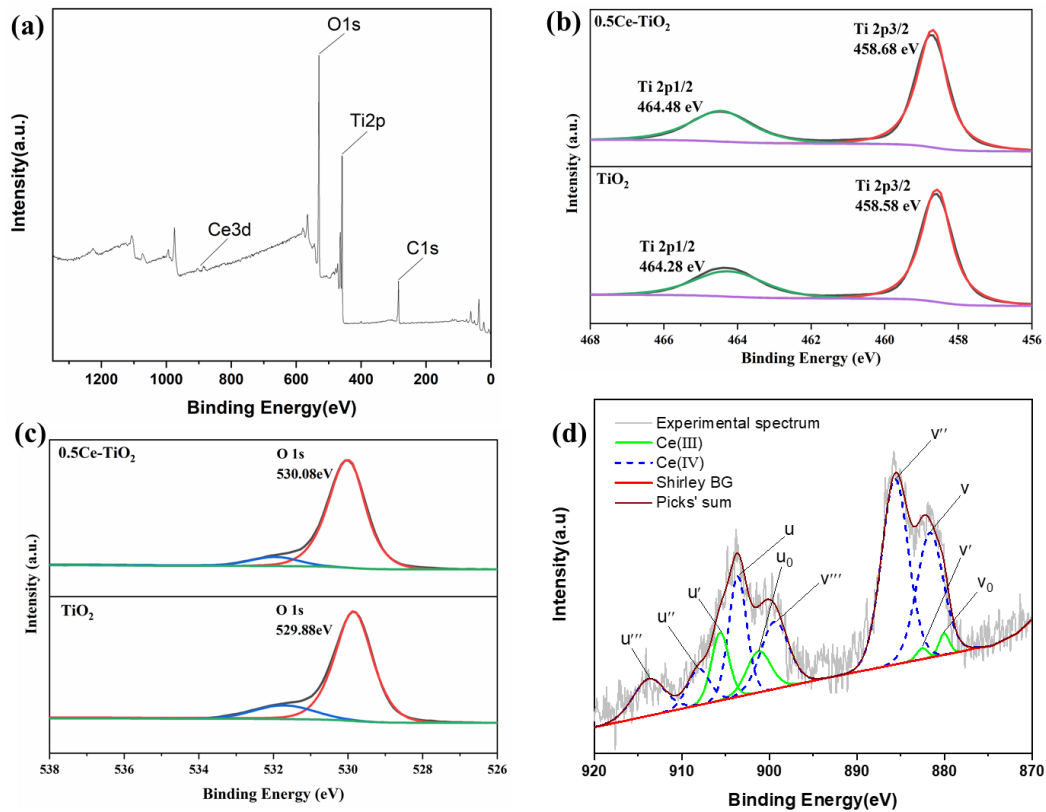

Figure 2. XPS spectra of 0.5Ce-TiO_2 samples: (**a**) the wide scan spectra, (**b**) Ti 2p, (**c**) O 1s and (**d**) Ce 3d.

Figure 2a demonstrates the full range survey XPS spectrum of 0.5Ce-TiO_2 sample. It contains O, Ti and C elements, with sharp photoelectron peaks appearing at binding energies of 531 (O 1s), 458 (Ti 2p) and 285 eV (C 1s). O and Ti are derived from the synthesized photocatalyst, while C 1s is derived from the anhydrous ethanol solvent added during the synthesis process, which fails to volatilize completely during drying and calcination and remains on the surface of the sample. However, it also shows that since there is low doping Ce content, the characterized peak of the Ce element is very weak.

Figure 2b shows the high resolution XPS spectra of Ti 2p for the synthesized sample 0.5Ce-TiO_2 and pure TiO_2. The TiO_2 exhibits two peaks at binding energies 458.58 eV (Ti 2p3/2) and 464.28 eV (Ti 2p1/2), confirming Ti mainly in the Ti^{4+} chemical state [19]. Compared with pure TiO_2, the two binding energies of Ti 2p after doping Ce show a slight shift for both the two spin orbitals Ti 2p3/2 (458.68 eV) and Ti 2p1/2 (464.48 eV), which indicates a strong interaction of Ti and Ce species [20]. The results suggest the changes in the Ti oxidation states (from Ti^{4+} to Ti^{3+}) and confirm that the Ce element is successfully doped into the TiO_2 structure. Figure 2c shows the O 1s high resolution spectra. The characteristic peak at 529.88 eV in pure TiO_2 is assigned to the crystal lattice oxygen O^{2-}. The main O 1s peak position for 0.5Ce-TiO_2 is slightly shifted to lower binding energy around 530.08 eV. The reason for peak shifts in O 1s and Ti 2p can be explained by the fact that transferring electrons from O 1s and Ti 2p orbitals to Ce 4f orbitals causes change in the charge densities of the O and Ti atoms [21].

Figure 2d shows the high resolution XPS spectrum of Ce 3d for the synthesized sample 0.5Ce-TiO_2. The spin orbitals coupling states of 3d5/2 and 3d3/2 are labelled with v and u, respectively. The XPS spectrum of the Ce 3d is relatively complex, mainly due to the

hybridization of O 2p and Ce 4f orbital electrons and the partial occupation of the 4f [21]. Hence, the spectrum is categorized into ten constituents. The binding energies of Ce 3d5/2 at 880.06, 881.67, 882.58, 885.66 and 899.39 eV are labelled with v_0, v, v′, v″ and v‴, while Ce 3d3/2 at 901.22, 903.62, 908.08, 904.12 and 913.74 eV are labelled with u_0, u, u′, u″ and u‴ [22]. The peaks at v_0, v′, u_0 and u′ are characteristic binding energies of Ce^{3+} configurations between the O 2p level and Ce 4f level. v′/u′ is related to the $Ce(3d^94f^2)$ $(O\ 2p^5)$ final state, and v_0/u_0 is assigned to the $Ce(3d^94f^1)$ $(O\ 2p^6)$ final state [23]. The peaks at v, v″, v‴, u, u″ and u‴ are attributed to Ce^{4+}. v‴/u‴ is related to the primary photoemission from $Ce(3d^94f^0)$ $(O\ 2p^6)$ final state, and v/u is related to the $Ce(3d^94f^1)$ $(O\ 2p^5)$ final state [24]. The v″/u″ is from the transfer of two electrons from the O 2p orbital to an empty Ce 4f orbital with the $Ce(3d^94f^1)$ $(O\ 2p^5)$ final state [25]. It is deduced that the surface of $0.5Ce-TiO_2$ is not fully oxidized due to the presence of Ce^{4+}/Ce^{3+}, and the Ce–O–Ti bond may be formed at the interstitial sites or interfaces between CeO_2 and Ce_2O_3, though their contents are too small to be detected by XRD [25].

2.1.2. FT-IR and UV-Vis DRS Analysis

Functional groups on the surface of the TiO_2, CeO_2 and $Ce-TiO_2$ catalyst were analyzed by Fourier Transform Infrared Spectrometer (FT-IR). The UV-vis diffuse reflectance spectra of the materials in the range of 200–800 nm were recorded. The results are shown in Figure 3.
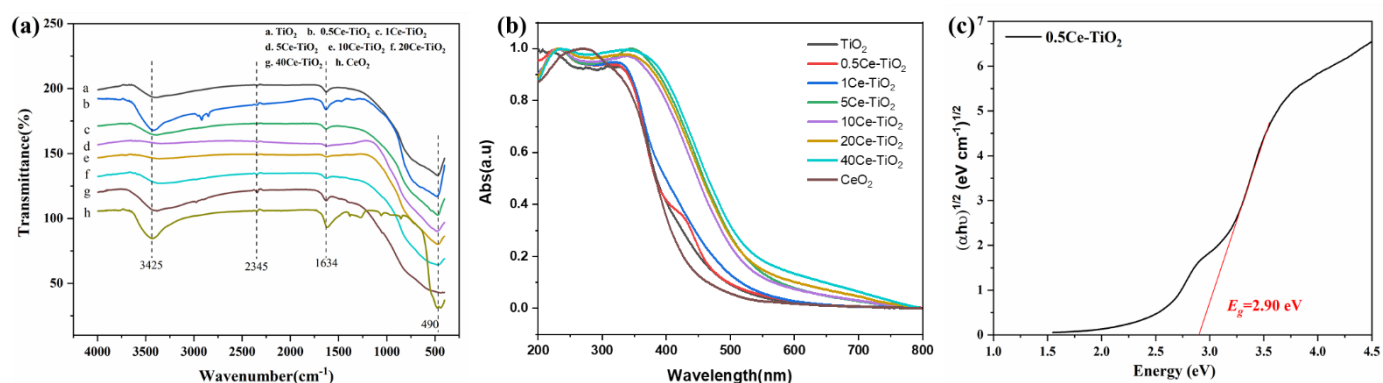

Figure 3. (**a**) FT-IR spectra of TiO_2, CeO_2 and $Ce-TiO_2$ samples. (**b**) UV-Vis absorption spectra of TiO_2, CeO_2 and $Ce-TiO_2$ with different Ce ion doping concentration. (**c**) The corresponding band gaps of $0.5Ce-TiO_2$.

We can see from Figure 3a that the three main characteristic absorption peaks of TiO_2 are at 490, 1634 and 3425 cm^{-1}, respectively, and the three characteristic absorption peaks correspond to the stretching vibration of the Ti-O-Ti bond in the TiO_2, and the bending vibration and stretching vibration of the O-H bond in the water molecules present on the surface [26–29]. Comparing the infrared absorption curves of TiO_2 doped with Ce, the TiO_2 characteristic absorption peaks in the composites doped with Ce are all present, and the absorption strength of the peaks at 3425 cm^{-1} is enhanced. The results are consistent with the previous reports [29]. Moreover, in the infrared absorption curve of the $Ce-TiO_2$, the characteristic absorption peak corresponding to the TiO_2 at 490 cm^{-1} is shifted, and the position of the peak appears at about 513 cm^{-1}. This may be because Ce enters the lattice of TiO_2 to form Ti-O-Ce bonds, causing effect on the stretching vibration of the original Ti-O-Ti bond. From the figure, we can also see that there is an absorption peak around 2345 cm^{-1} corresponding to CO_2. The characteristic absorption peak indicates that ethanol did not completely volatilize during the synthesis of the material, and the remaining small amount of inorganic carbon was oxidized to CO_2 during drying.

According to the spectra, TiO_2 mainly absorbs ultraviolet (UV) light, and its maximum wavelength is 393 nm. The maximum absorption wavelength of all the $Ce-TiO_2$ catalyst samples is shifted to the visible range of 400–600 nm, which expands the range of its absorption spectrum. Moreover, with the increase of Ce content, the red shift of the catalyst

samples is more obvious. Among all Ce-TiO$_2$ catalyst samples, the red shift of doped metal Ce content is the largest when the content of Ce is 40%. The absorbance of pure TiO$_2$ is from the electron transition from O 2p to Ti 3d state. The red shift of Ce-doped TiO$_2$ may be caused by the formation a new electronic state, which reduces the distance of charge transfer between 4f electrons of Ce ions and the conduction or valence band in the TiO$_2$ bandgap, enhancing the photocatalytic activity [30]. Li et al. have ascribed to Ce^{4+}/Ce^{3+} ions as electron scavengers to trap the electrons of TiO$_2$ and the Ce 4f level as an interfacial charge transfer and elimination of electron-hole recombination [24].

Comparing with all catalyst samples in the UV region of 200–400 nm, it is found that the doping of Ce can improve the absorbance of TiO$_2$, and the absorbance of TiO$_2$ increases with the increase of the doping amount of Ce. Band gaps estimated from Tauc transformations of the absorbance spectra are shown in Figure 3c. The band gap (E_g) is calculated mainly by the following formula [31]:

$$(\alpha h\nu)^{1/2} = K(h\nu - E_g) \tag{1}$$

where $h\nu$ represents photon energy, α represents absorption coefficient, E_g represents band gap energy and K is a constant. It can be seen from Figure 3c that the band gap width of the synthesized 0.5Ce-TiO$_2$ sample is 2.9 eV, less than that of TiO$_2$ (E_g = 3.2 eV). The results indicate that doping Ce in TiO$_2$ significantly reduces the band gap energy and effectively inhibits the recombination of photogenerated electrons-holes.

2.2. Photocatalytic Degradation of Deoxynivalenol

2.2.1. Evaluation of the Effectiveness of DON Degradation

The effectiveness of Ce-TiO$_2$ photocatalytic degradation DON under UV light (λ = 254 nm) and the total organic carbon (TOC) changing trends during the reaction of photocatalytic degradation DON in aqueous solution using 0.5Ce-TiO$_2$ are shown in Figure 4.
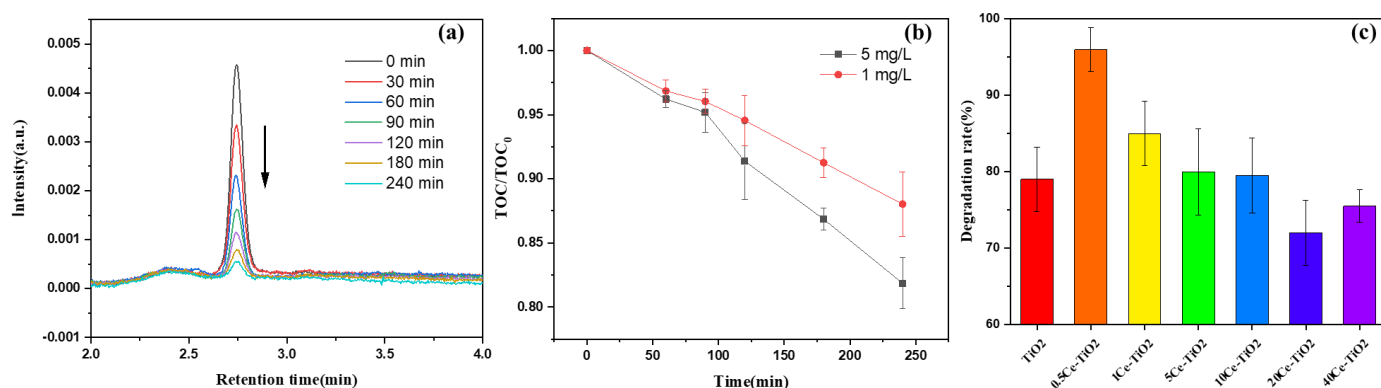

Figure 4. (**a**) HPLC chromatogram of DON photodegradation using 0.5Ce-TiO$_2$. (**b**) TOC removal in DON aqueous solution of different initial concentration. (**c**) The degradation rate of different photocatalysts under UV light irradiation for DON removal after 240 min.

The rapid photocatalytic degradation of DON over 0.5Ce-TiO$_2$ nanomaterials was clearly seen by using High Performance Liquid Chromatography (HPLC), as shown in Figure 4a. The HPLC chromatograms show decreasing DON peaks at retention time 2.74 min with prolonging irradiation time. The Figure 4c shows the different photocatalytic degradation effects of Ce-TiO$_2$ with different Ce doping content and pure TiO$_2$. The optimum doping amount of Ce is 0.5% in our study. The degradation rate of the DON aqueous solution at 5 mg/L can reach 96% using 0.5Ce-TiO$_2$ under UV light irradiation after 240 min. The photocatalytic degradation effect is higher than 85% under the same conditions. The results indicate that the small CeO$_2$ particles produced on the TiO$_2$ particles caused by Ce doping play a co-catalytic effect on DON degradation. The removal effects of 5Ce-TiO$_2$ and 10Ce-TiO$_2$ are equivalent to pure TiO$_2$. However, the degradation

rate of 10Ce-TiO$_2$ and 40Ce-TiO$_2$ are lower than that of TiO$_2$. The main reason may be that excessive Ce destroy the TiO$_2$ lattice structure and decrease the photoactivity of the nanomaterials, although the light absorption range redshifts [32]. The results indicate that 0.5Ce-TiO$_2$ has superior photocatalytic activity for DON removal under UV light (λ = 254 nm) irradiation, which is even better than that of the traditional photocatalyst TiO$_2$.

In the course of the degradation, the measurement of TOC is an important embodiment of the mineralization reaction and the mineralization degree. DON aqueous solution with initial concentrations of 1 mg/L and 5 mg/L were selected here. It can be seen from Figure 4b that the TOC values are gradually decreasing with prolonging the photocatalytic reaction, which means that the mineralization rate of the DON aqueous solution is increasing with the reaction time increasing. The results indicate that more and more DON molecules are further oxidized to H$_2$O and CO$_2$ completely. The TOC/TOC$_0$ ratio of 5 mg/L is less than that of 1 mg/L resulted from more molecules involved in the degradation reaction in the high concentration of the DON aqueous solution.

2.2.2. Free Radical Trapping Experiments and Photocatalytic Degradation Mechanism

To explore the main active substances in the process of DON degradation, the active material capture experiments were carried out. We choose EDTA-2Na as hole (h$^+$) scavenger [33], tert-butanol as the hydroxyl radical ($\bullet$OH) [34] and nitrogen (N$_2$) bubbling was used to superoxide radicals ($\bullet$O$_2^-$) trapping agents. The results are shown in Figure 5a.
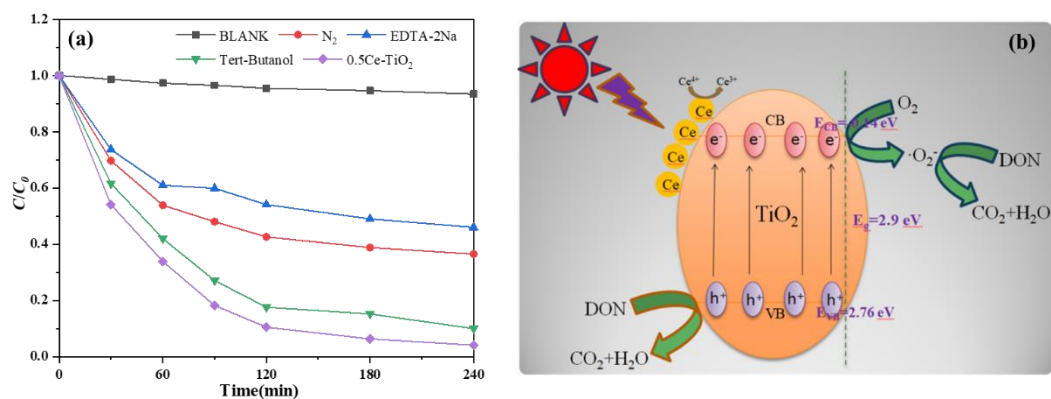

Figure 5. (**a**) The various scavengers' effects on the photocatalytic degradation of DON using 0.5Ce-TiO$_2$. (**b**) Schematic illustration for the charge separation and transfer of Ce-TiO$_2$ in the process of DON degradation under UV light irradiation.

From Figure 5a, the photocatalytic activity of 0.5Ce-TiO$_2$ decreases largely by the addition of hole scavenger (EDTA-2Na), while no significant decrease was observed by the addition of $\bullet$OH scavengers, indicating that $\bullet$OH are not the main oxidative species affecting catalytic degradation. That is, the hole plays a more key role in the photocatalytic degradation reaction than $\bullet$OH in the UV light irradiation [35]. In addition, the degradation efficiency of DON using 0.5Ce-TiO$_2$ is obviously reduced with the anoxic solution, indicating that O$_2$ is another more important role in the photodegradation reaction that produces more $\bullet$O$_2^-$, which is consistent with the previous study [36]. Based on all the results above, we can conclude that the photooxidation mechanism occurring on the surface of 0.5Ce-TiO$_2$ may involve in the direct oxidizing reaction of DON with $\bullet$O$_2^-$ and holes. The photocatalytic degradation mechanism of the 0.5Ce-TiO$_2$ sample may involve the oxidation process of holes and $\bullet$O$_2^-$.

The photocatalytic degradation mechanism for DON removal using Ce-TiO$_2$ nanomaterials synthesized in this experiment for DON are shown in Figure 5b. The electrons in the valence band (VB) of the Ce-TiO$_2$ sample are excited to the conduction band (CB) under the irradiation of UV light. The number of holes on VB is the same as the number of electrons on CB. Under general conditions, photogenerated electrons-hole carriers are easily inclined to recombine, resulting in only a small part of the electrons involved in the

catalytic degradation process [37]. The band position of doped samples is mainly calculated by the following formulas [38]:

$$E_{VB} = \chi - E^e + 0.5E_g \tag{2}$$

$$E_{CB} = \chi - E^e - 0.5E_g \tag{3}$$

where E_{VB}, E_{CB}, χ and the E_g are the VB edge potential, CB edge potential, Sanderson electronegativity and the band gap of the photocatalysts. The value of χ for TiO_2 is 5.81 eV, and E^e represents the free electron energy on the hydrogen scale, with a value of 4.5 eV. According to the above formula, the E_{CB} of Ce-TiO_2 is -0.14 eV and the E_{VB} is 2.76 eV. In this material, Ce dopants into the TiO_2 lattice introduce new impurity levels (empty Ce 4f) with a smaller band gap close to the Ti 3d conduction band of TiO_2 [32]. Under light illumination, the distance of the excited charge carrier transfer from Ti 3d of TiO_2 to Ce 4f level is narrowed [39], which can reduce the charge carrier's recombination rate [40]. In addition, the photogenerated electrons on the conduction band react with O_2 to form $\bullet O_2{}^-$, and holes in VB react with DON to form CO_2 and H_2O. The reaction formula is:

$$e^- + O_2 \rightarrow \bullet O_2{}^- \tag{4}$$

$$h^+ + \text{-OH} \rightarrow \bullet OH \tag{5}$$

$$DON + h^+ \rightarrow CO_2 + H_2O \tag{6}$$

$$DON + \bullet O_2{}^- \rightarrow CO_2 + H_2O \tag{7}$$

2.2.3. Intermediate Products of Don Degradation and Possible Photodegradation Pathway

The intermediate products of DON photocatalytic degradation were analyzed using by Ultra Performance Liquid Chromatography coupled with Quadrupole Time-of-flight Mass Spectrometry (UPLC-QTOF/MS) (ESI$^+$ mode).

As shown in Figure 6a, Extracted Ion Chromatogram (XIC) shows the two intermediate products' peaks. The two intermediates chemical structures P1 $C_5H_8O_3$ (m/z theoretical 117.06, experimental 117.07) and P2 $C_{17}H_{18}O_6$ (m/z theoretical 319.12, experimental 319.12) are identified by comparing with the DON (m/z theoretical 297.00) molecule, as shown Figure 6b. We speculate that P1 and P2 structures are from a possible unstable intermediates (IP1) six-membered ring compound via opening loop with C1-C2 bond fractures and by removing the five-membered ring. The five-membered ring with a 12,13-epoxy group is one of the main toxic functional groups in DON [41]. The reaction can eliminate the toxicity of DON. However, we did not find that the carbonyl-containing intermediate product ion (m/z 303.09) formed by the epoxy ring group destroyed, which is different from the previous study [42] due to the strong oxidizing ability. Then, IP1 dehydrates to form the relatively stable compound IP2. Two possible reaction pathways may exist. One is that IP2 continue to be oxidized to form P1. The other one is that the two IP2 molecules are coupled to form P2. The intensity changing trends of the molecular ion peak of [DON+H]$^+$, [P1+H]$^+$ and [P2+H]$^+$ with the reaction time are shown in Figure 6c. Because TOC content gradually decreases with the reaction time increasing, DON is further oxidized and mineralized to CO_2 and H_2O completely. The possible pathway that intermediate products P1 and P2 generated from DON molecular break, continued to react and finally disappeared with the photocatalytic degradation reaction is speculated and shown in Figure 6d.
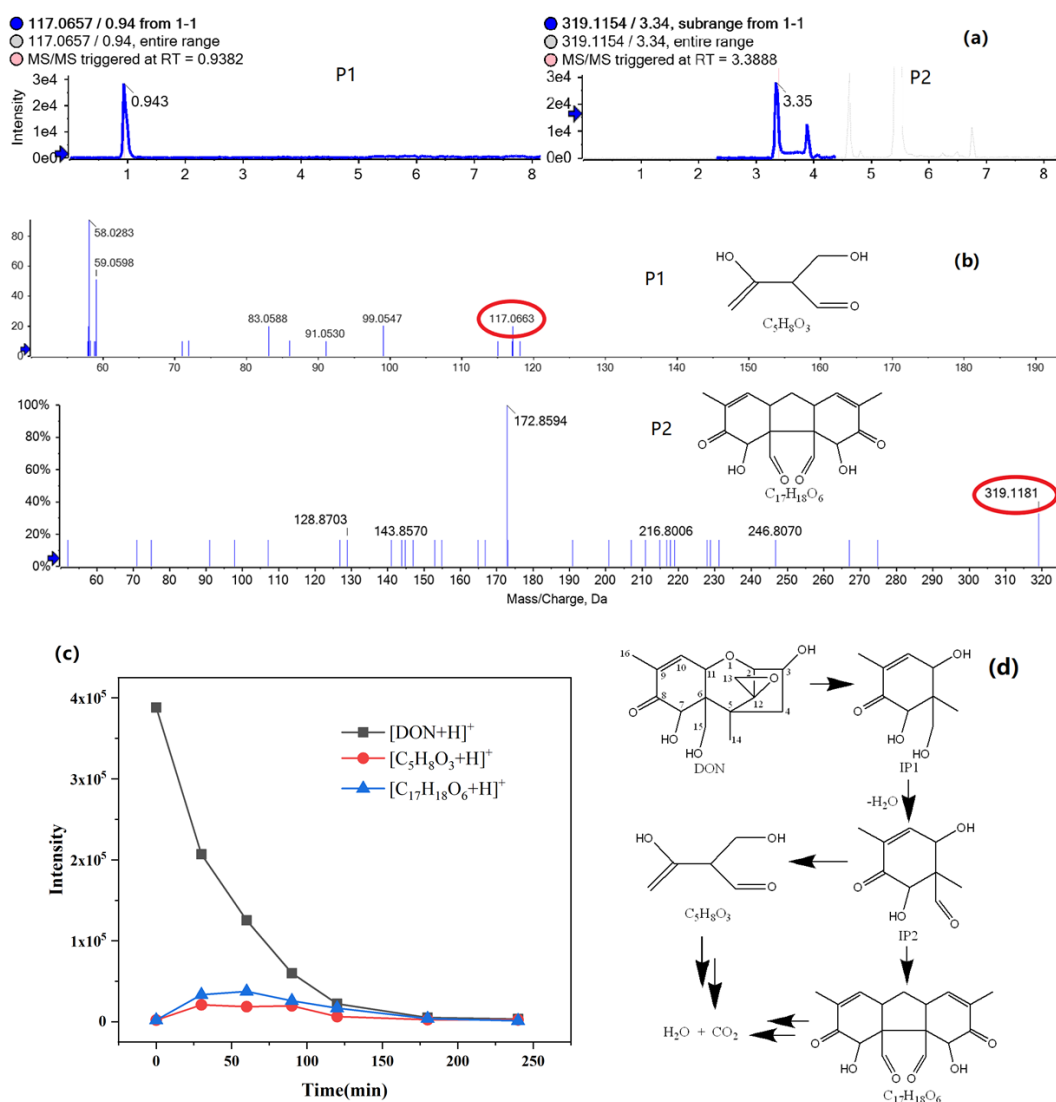
Figure 6. (**a**) Extracted Ion Chromatogram (XIC) of intermediate products P1 and P2. (**b**) MS/MS spectrum of intermediate products P1 and P2. (**c**) The intensity changing trends of the molecular ion peak of [DON+H]$^+$, [P1+H]$^+$ and [P2+H]$^+$ with the reaction time. (**d**) The pathway of DON degradation.

3. Conclusions

In conclusion, TiO$_2$ photocatalytic nanomaterials doped with Ce were successfully prepared by the sol-gel method. In these synthesized materials, 0.5Ce-TiO$_2$ shows superior photocatalytic activity for DON removal in aqueous solution under UV light irradiation (λ = 254 nm). The free radical trapping experiments indicate that the photogenerated h$^+$ and •O$_2$$^-$ are the two main active substances for DON photocatalytic degradation. The two possible degradation intermediate products C$_5$H$_8$O$_3$ (m/z 117.07) and C$_{17}$H$_{18}$O$_6$ (m/z 319.12) were identified, which indicates that the main toxic groups in the DON molecule were destroyed. This work provides an efficient and mild method to reduce DON contamination. In order to further evaluate the feasibility of this method, the study on toxicity of DON degradation products is ongoing.

4. Materials and Methods

4.1. Materials

Tertbutyl titanate (TBOT), cerium nitrate hexahydrate (Ce(NO$_3$)$_3$•6H$_2$O, 99%), tert-butyl alcohol (TBA), EDTA-2Na and acetic acid were purchased from Shanghai Titan Technology Co., Ltd. Water used in the experiment was ultrapure water prepared from the

Milli-Q system (Millipore, Billerica, MA, USA). Acetonitrile and methanol (mass spectrum grade) were purchased from Fisher Chemical.

4.2. Synthesis of Ce-TiO$_2$, TiO$_2$ and CeO$_2$

Ce-dropped TiO$_2$ (Ce-TiO$_2$) based catalysts were prepared using the sol-gel method. In the study, tertbutyl titanate (TBOT) and cerium nitrate hexahydrate (Ce(NO$_3$)$_3$•6H$_2$O) were used as the reaction precursors. The typical synthetic procedure was as follows: first, 15 mL TBOT and little amounts of acetic acid were dissolved in 30 mL absolute ethanol to make the solution A. The solution B was cerium nitrate hexahydrate aqueous solution. Solution B was dropped into solution A slowly with vigorous stirring. The mixed solution continued to stir, and the solution became sol and gel. The gel stood for 12 h, and then was dried at 120 °C in an oven; finally, it was calcined at 550 °C for 3 h. The product was Ce-TiO$_2$. Using the same synthesis procedure, the product with different proportion was obtained by only changing the content of cerium nitrate (the Ce contents were varied as Ce: Ti = 0.5, 1, 5, 10, 20 and 40% in molar ratio) and was marked as 0.5Ce-TiO$_2$, 1Ce-TiO$_2$, 5Ce-TiO$_2$, 10Ce-TiO$_2$, 20Ce-TiO$_2$ and 40Ce-TiO$_2$, respectively. In addition, pure TiO$_2$ nanomaterials were synthesized without adding cerium nitrate as a control. The CeO$_2$ catalyst was also prepared by sol-gel method [43].

4.3. Characterization of Catalysts

The crystal structure of the sample was determined by X-ray diffraction (Bruker D8 ADVANCE, Germany), with Cu Kα radiation as the X-ray source, and operated at 40 kV and 40 mA. The 2θ scan range was 20–85° with a step size of 0.02°. Morphology and structure of catalysts were observed using high-resolution transmission electron microscopy instruments (JEM-2100F, Japan). X-ray photoelectron spectroscopy (XPS) studies were performed with a Escalab 250Xi spectrometer (ThermoFisher, MA, USA), using a mono-chromatic Al Kα source. The infrared spectra were recorded on the Nicolet iS5 FT-IR Spectrometer (Thermo Scientific, WI, USA). The UV-Vis diffuse reflectance spectra of 200–800 nm were recorded on the Shimadzu UV 3600plus (Shimadzu, Japan).

4.4. DON Photocatalytic Tests

Photocatalytic tests were carried out in photochemical reaction apparatus, and the tests were performed using a UV lamp (254 nm). The initial concentration of DON solution was 5 mg/L. Before the light irradiation, 2.5 mg catalyst was added to 20 mL of DON solution and kept in the dark for 30 min to reach the adsorption-desorption equilibrium. After different irradiation times (30 min, 60 min, 90 min, 120 min, 180 min and 240 min), 1 mL of suspension was collected and centrifuged at high speed. The upper liquid was filtered through a 0.22 μm filter membrane and was analyzed. The concentration of DON was determined by Acquity Ultra Performance LC (Waters, Milford, MA, USA) equipped with a Waters Acquity BEH C18 column (1.7 μm, 2.1 × 100 nm) and with an isocratic mobile phase composed of methanol-water (20:80) at a flow rate of 0.25 mL/min. The DON degradation rate was calculated by the following formula.

$$\eta(\%) = (C_0 - C_t)/C_0 \times 100 \tag{8}$$

where C_0 represents the initial concentration of DON, and C_t represents the concentration of DON after photocatalytic degradation.

Seven DON aqueous solutions of 20 mL with the same initial concentration 1 mg/L and 5 mg/L were, respectively, irradiated at different irradiation times (0 min, 30 min, 60 min, 90 min, 120 min, 180 min and 240 min) and directly submitted to TOC analysis. The TOC content was determined by Total Organic Carbon Analyzer TOC-L CPH Basic System (Shimadzu Co. Ltd., Kyoto, Japan).

To investigate the photocatalytic mechanism of DON degradation, the active species trapping experiment was performed with three different active substance capture agents

(N$_2$, ethylenediaminetetraacetic acid disodium salt dihydrate (EDTA-2Na) and tert-butyl alcohol). The other conditions remain unchanged in this experiment.

4.5. Degraded Intermediate Products Analysis

The identification of the intermediate products of DON was performed by AB SCIEX 5600 Triple TOF mass spectrometer (Foster City, MA, USA). A Waters Acquity BEH C18 column (1.7 μm, 2.1 × 100 mm) was used for chromatographic separation at a flow rate of 0.3 mL/min. The mobile phase consisted of methanol (A) and water (B). A linear gradient elution program was used as follows: 0 –2.0 min, 5% A; 2.0–15.0 min, 5–95% A; 15.0–17.0 min, 95% A; 17.0–17.1 min, 95–5% A; 17.1–20.0 min, 5% A. The mass spectrometer conditions were as follows: ion spray voltage, 5.5 kV; block source temperature, 500 °C; ion source gas 1 pressure, 50 psi; ion source gas 2 pressure, 50 psi; curtain gas pressure, 35 psi. TOF/MS scan was performed in the mass range of m/z 50–400 with the collision energies of 10 and 45 eV. Data processes were performed using PeakView version 2.1 and MasterView version 1.0 (AB Sciex, Framingham, MA, USA).

Author Contributions: Conceptualization, X.Y. and S.C.; methodology, P.H. and Z.Z.; software, P.H.; validation, P.H., Z.Z. and H.E.; formal analysis, M.Z.; investigation, J.W.; resources, J.W. and J.Y.; data curation, P.H.; writing—original draft preparation, P.H.; writing—review and editing, X.Y. and Y.T.; visualization, P.H. and Y.T.; supervision, X.Y. and S.C.; project administration, X.Y.; funding acquisition, X.Y. and J.W. All authors have read and agreed to the published version of the manuscript.

Conflicts of Interest: The authors declare no conflict of interest.

References

1. Wu, S.; Wang, F.; Li, Q.; Zhou, Y.; He, C.; Duan, N. Detoxification of don by photocatalytic degradation and quality evaluation of wheat. *RSC Adv.* **2019**, *9*, 34351–34358. [CrossRef]
2. Authority, E.F.S. Deoxynivalenol in food and feed: Occurrence and exposure. *EFSA J.* **2013**, *11*, 3379.
3. Pestka, J.J. Deoxynivalenol: Mechanisms of action, human exposure, and toxicological relevance. *Arch. Toxicol* **2010**, *84*, 663–679. [CrossRef]
4. Zhao, Z.; Song, S.; Liu, N.; Rao, Q.; Hou, J.; De Saeger, S.; Wu, A. Large-scale preparation and multi-dimensional characterization of high-purity mycotoxin deoxynivalenol in rice culture inoculated with fusarium graminearum. *Anal. Methods* **2014**, *6*, 6651–6657. [CrossRef]
5. Pronyk, C.; Cenkowski, S.; Abramson, D. Superheated steam reduction of deoxynivalenol in naturally contaminated wheat kernels. *Food Control* **2006**, *17*, 789–796. [CrossRef]
6. Bretz, M.; Beyer, M.; Cramer, B.; Knecht, A.; Humpf, H.-U. Thermal degradation of the fusarium mycotoxin deoxynivalenol. *J. Agric. Food Chem.* **2006**, *54*, 6445–6451. [CrossRef] [PubMed]
7. Zhu, Y.; Hassan, Y.I.; Lepp, D.; Shao, S.; Zhou, T. Strategies and methodologies for developing microbial detoxification systems to mitigate mycotoxins. *Toxins* **2017**, *9*, 130. [CrossRef] [PubMed]
8. Yin, X.; Zhu, Z.; Zhou, Y.; Ji, F.; Yao, Z.; Shi, J.; Xu, J. Complete genome sequence of deoxynivalenol-degrading bacterium devosia sp. Strain a16. *J. Biotechnol.* **2016**, *218*, 21–22. [CrossRef]
9. Bhatkhande, D.S.; Pangarkar, V.G.; Beenackers, A.A.C.M. Photocatalytic degradation for environmental applications—A review. *J. Chem. Technol. Biotechnol. Int. Res. Process Environ. Clean Technol.* **2002**, *77*, 102–116. [CrossRef]
10. Wang, H.; Mao, J.; Zhang, Z.; Zhang, Q.; Zhang, L.; Zhang, W.; Li, P. Photocatalytic degradation of deoxynivalenol over dendritic-like α-fe2o3 under visible light irradiation. *Toxins* **2019**, *11*, 105. [CrossRef]
11. Zhou, Y.; Wu, S.; Wang, F.; Li, Q.; He, C.; Duan, N.; Wang, Z. Assessing the toxicity in vitro of degradation products from deoxynivalenol photocatalytic degradation by using upconversion nanoparticlesnanoparticles@TiO$_2$ composite. *Chemosphere* **2020**, *238*, 124648. [CrossRef]
12. Wang, F.; Feng, L.; Qin, Y.; Zhao, T.; Luo, H.; Zhu, J. Dual functional SiO$_2$@TiO$_2$ photonic crystals for dazzling structural colors and enhanced photocatalytic activity. *J. Mater. Chem. C* **2019**, *7*, 11972–11983. [CrossRef]
13. Yan, N.; Zhu, Z.; Zhang, J.; Zhao, Z.; Liu, Q. Preparation and properties of ce-doped TiO$_2$ photocatalyst. *Mater. Res. Bull.* **2012**, *47*, 1869–1873. [CrossRef]

14. Siriwong, C.; Wetchakun, N.; Inceesungvorn, B.; Channei, D.; Samerjai, T.; Phanichphant, S. Doped-metal oxide nanoparticles for use as photocatalysts. *Prog. Cryst. Growth Charact. Mater.* **2012**, *58*, 145–163. [CrossRef]
15. Ranjit, K.T.; Willner, I.; Bossmann, S.H.; Braun, A.M. Lanthanide oxide doped titanium dioxide photocatalysts: Effective photocatalysts for the enhanced degradation of salicylic acid and t-cinnamic acid. *J. Catal.* **2001**, *204*, 305–313. [CrossRef]
16. Liu, Z.; Guo, B.; Hong, L.; Jiang, H. Preparation and characterization of cerium oxide doped TiO_2 nanoparticles. *J. Phys. Chem. Solids* **2005**, *66*, 161–167. [CrossRef]
17. Gionco, C.; Paganini, M.C.; Agnoli, S.; Reeder, A.E.; Giamello, E. Structural and spectroscopic characterization of CeO_2–TiO_2 mixed oxides. *J. Mater. Chem. A* **2013**, *1*, 10918–10926. [CrossRef]
18. Wang, B.; Zhang, G.; Sun, Z.; Zheng, S.; Frost, R.L. A comparative study about the influence of metal ions (Ce, La and V) doping on the solar-light-induced photodegradation toward rhodamine B. *J. Environ. Chem. Eng.* **2015**, *3*, 1444–1451. [CrossRef]
19. Anandan, S.; Rao, T.N.; Sathish, M.; Rangappa, D.; Honma, I.; Miyauchi, M. Superhydrophilic graphene-loaded TiO_2 thin film for self-cleaning applications. *ACS Appl. Mater. Interfaces* **2013**, *5*, 207–212. [CrossRef]
20. Zhang, J.; Hu, Y.; Zheng, H.; Zhang, P. Hierarchical z-scheme 1D/2D architecture with TiO_2 nanowires decorated by MnO_2 nanosheets for efficient adsorption and full spectrum photocatalytic degradation of organic pollutants. *Catal. Sci. Technol.* **2020**, *10*, 3603–3612. [CrossRef]
21. Lu, H.; Zhuang, J.; Ma, Z.; Zhou, W.; Xia, H.; Xiao, Z.; Zhang, H.; Haimin, L. Crystal recombination control by using ce doped in mesoporous TiO_2 for efficient perovskite solar cells. *RSC Adv.* **2019**, *9*, 1075–1083. [CrossRef]
22. Chang, L.-H.; Sasirekha, N.; Chen, Y.-W.; Wang, W.-J. Preferential oxidation of CO in H_2 stream over au/MnO_2–CeO_2 catalysts. *Ind. Eng. Chem. Res.* **2006**, *45*, 4927–4935. [CrossRef]
23. Li, F.B.; Li, X.Z.; Hou, M.F.; Cheah, K.W.; Choy, W.C.H. Enhanced photocatalytic activity of Ce^{3+}–TiO_2 for 2-mercaptobenzothiazole degradation in aqueous suspension for odour control. *Appl. Catal. A Gen.* **2005**, *285*, 181–189. [CrossRef]
24. Li, R.; Dong, G.; Chen, G. Synthesis, characterization and performance of ternary doped Cu–Ce–B/TiO_2 nanotubes on the photocatalytic removal of nitrogen oxides. *New J. Chem.* **2015**, *39*, 6854–6863. [CrossRef]
25. Tuyen, L.T.T.; Quang, D.A.; Tam Toan, T.T.; Tung, T.Q.; Hoa, T.T.; Mau, T.X.; Khieu, D.Q. Synthesis of CeO_2/TiO_2 nanotubes and heterogeneous photocatalytic degradation of methylene blue. *J. Environ. Chem. Eng.* **2018**, *6*, 5999–6011. [CrossRef]
26. Huang, Z.; Sun, Q.; Lv, K.; Zhang, Z.; Li, M.; Li, B. Effect of contact interface between TiO_2 and g-C_3N_4 on the photoreactivity of g-C_3N_4/TiO_2 photocatalyst: (0 0 1) vs. (1 0 1) facets of TiO_2. *Appl. Catal. B Environ.* **2015**, *164*, 420–427. [CrossRef]
27. Wang, J.; Huang, J.; Xie, H.; Qu, A. Synthesis of g-C_3N_4/TiO_2 with enhanced photocatalytic activity for H_2 evolution by a simple method. *Int. J. Hydrogen Energy* **2014**, *39*, 6354–6363. [CrossRef]
28. Pillai, S.C.; Periyat, P.; George, R.; McCormack, D.; Seery, M.; Hayden, H.; Colreavy, J.; Corr, D.; Hinder, S.J. Synthesis of high-temperature stable anatase TiO_2 photocatalyst. *J. Phys. Chem. C* **2007**, *111*, 1605–1611. [CrossRef]
29. Malik, A.; Hameed, S.; Siddiqui, M.; Haque, M.; Muneer, M. Influence of ce doping on the electrical and optical properties of TiO_2 and its photocatalytic activity for the degradation of remazol brilliant blue R. *Int. J. Photoenergy* **2013**, *2013*, 1–9. [CrossRef]
30. Xu, Y.-h.; Zeng, Z.-x. The preparation, characterization, and photocatalytic activities of Ce-TiO_2/SiO_2. *J. Mol. Catal. A Chem.* **2008**, *279*, 77–81. [CrossRef]
31. Hao, R.; Wang, G.; Jiang, C.; Tang, H.; Xu, Q. In situ hydrothermal synthesis of g-C_3N_4 /TiO_2 heterojunction photocatalysts with high specific surface area for rhodamine b degradation. *Appl. Surf. Sci.* **2017**, *411*, 400–410. [CrossRef]
32. Shayegan, Z.; Haghighat, F.; Lee, C.-S. Surface fluorinated ce-doped TiO_2 nanostructure photocatalyst: A trap and remove strategy to enhance the voc removal from indoor air environment. *Chem. Eng. J.* **2020**, *401*, 125932. [CrossRef]
33. Zhou, J.; Deng, C.; Si, S.; Shi, Y.; Zhao, X. Study on the effect of edta on the photocatalytic reduction of mercury onto nanocrystalline titania using quartz crystal microbalance and differential pulse voltammetry. *Electrochim. Acta* **2011**, *56*, 2062–2067. [CrossRef]
34. Hyunjoo Lee, W.C. Photocatalytic oxidation of arsenite in TiO_2 suspension: Kinetics and mechanisms. *Environ. Sci. Technol.* **2002**, *36*, 3872–3878.
35. Yang, B.; Zheng, J.; Li, W.; Wang, R.; Li, D.; Guo, X.; Rodriguez, R.D.; Jia, X. Engineering z-scheme TiO_2-ov-biocl via oxygen vacancy for enhanced photocatalytic degradation of imidacloprid. *Dalton Trans.* **2020**, *49*, 11010–11018. [CrossRef] [PubMed]
36. Bai, X.; Sun, C.; Liu, D.; Luo, X.; Li, D.; Wang, J.; Wang, N.; Chang, X.; Zong, R.; Zhu, Y. Photocatalytic degradation of deoxynivalenol using graphene/zno hybrids in aqueous suspension. *Appl. Catal. B Environ.* **2017**, *204*, 11–20. [CrossRef]
37. Tahir, M.; Cao, C.; Butt, F.K.; Idrees, F.; Mahmood, N.; Ali, Z.; Aslam, I.; Tanveer, M.; Rizwan, M.; Mahmood, T. Tubular graphitic-C_3N_4: A prospective material for energy storage and green photocatalysis. *J. Mater. Chem. A* **2013**, *1*, 13949–13955. [CrossRef]
38. Uddin, M.T.; Hoque, M.E.; Chandra Bhoumick, M. Facile one-pot synthesis of heterostructure SnO_2/ZnO photocatalyst for enhanced photocatalytic degradation of organic dye. *RSC Adv.* **2020**, *10*, 23554–23565. [CrossRef]
39. Xu, J.; Ao, Y.; Fu, D.; Yuan, C. Study on photocatalytic performance and degradation kinetics of x-3b with lanthanide-modified titanium dioxide under solar and uv illumination. *J. Hazard. Mater.* **2009**, *164*, 762–768. [CrossRef] [PubMed]
40. Liu, T.-X.; Li, X.-Z.; Li, F.-B. Enhanced photocatalytic activity of Ce^{3+}-TiO_2 hydrosols in aqueous and gaseous phases. *Chem. Eng. J.* **2010**, *157*, 475–482. [CrossRef]
41. Nagy, C.M.; Fejer, S.N.; Berek, L.; Molnar, J.; Viskolcz, B. Hydrogen bondings in deoxynivalenol (don) conformations—A density functional study. *J. Mol. Struct.* **2005**, *726*, 55–59. [CrossRef]

42. Cheng, L.; Jiang, T.; Zhang, J. Photoelectrocatalytic degradation of deoxynivalenol on CuO-Cu$_2$O/WO$_3$ ternary film: Mechanism and reaction pathways. *Sci. Total Environ.* **2021**, *776*, 145840. [CrossRef] [PubMed]
43. Periyat, P.; Laffir, F.; Tofail, S.A.M.; Magner, E. A facile aqueous sol–gel method for high surface area nanocrystalline CeO$_2$. *RSC Adv.* **2011**, *1*, 1794–1798. [CrossRef]